

Theory of Caroli-de Gennes-Matricon analogs in full-shell nanowires

Pablo San-Jose,¹ Carlos Payá,¹ C. M. Marcus,² S. Vaitiekėnas,² and Elsa Prada¹

¹*Instituto de Ciencia de Materiales de Madrid, Consejo Superior de Investigaciones Científicas (ICMM-CSIC), Madrid, Spain*

²*Center for Quantum Devices, Niels Bohr Institute, University of Copenhagen, 2100 Copenhagen, Denmark*

(Dated: July 18, 2022)

Full-shell nanowires are hybrid nanostructures consisting of a semiconducting core encapsulated in an epitaxial superconducting shell. When subject to an external magnetic flux, they exhibit the Little-Parks (LP) phenomenon of flux-modulated superconductivity, an effect connected to the physics of Abrikosov vortex lines in type-II superconductors. We show that full-shell nanowires can host subgap states that are a variant of the Caroli-de Gennes-Matricon (CdGM) states in vortices. These CdGM analogs are in fact shell-induced Van Hove singularities in propagating core subbands. We elucidate their structure, parameter dependence and behavior in tunneling spectroscopy through a series of models of growing complexity. We show through microscopic numerical simulations that they exhibit a characteristic skewness towards high magnetic fields inside non-zero LP lobes resulting from the interplay of three ingredients. First, core subbands exhibit a diamagnetic response, so that they disperse with flux depending on their generalized angular momentum. Second, the band bending at the core/shell interface induces a ring-like profile on the CdGM analog state wavefunctions with average radius smaller than the core radius. And last, degeneracy points emerge where all the CdGM Van Hove singularities coalesce. This happens when the flux threading each wavefunction is equal to an integer multiple of the flux quantum, a condition that shifts the degeneracy points away from the center of the LP lobes, skewing the CdGM analogs. Our analysis unlocks a transparent analytical description that allows to extract precise microscopic information about the nanowire by measuring the energy and skewness of CdGM analogs.

I. INTRODUCTION

Full-shell nanowires comprised of semiconducting nanowires fully encapsulated in a thin superconducting layer, or shell, have been recently introduced in the context of topological superconductivity¹⁻⁴. These wires could present several advantages for the generation and detection of Majorana bound states (MBSs) as compared to partial-shell ones, where the superconducting coating is limited to some facets of the nanowire⁵⁻⁹. In the full-shell case the trigger of the topological phase transition is the magnetic flux threading the nanowire produced by an external axial magnetic field, whereas in the partial-shell devices following the original proposal^{10,11}, it is the Zeeman effect. Partial-shell nanowires, sometimes dubbed Majorana nanowires, have been exhaustively analyzed since 2010, whereas the full-shell variant has only more recently began being explored.

The interest of full-shell hybrid nanowires, however, extends beyond their possible relevance for topological superconductivity. The doubly connected geometry of the superconducting shell makes them a versatile hybrid system with very rich physics¹²⁻¹⁵. In the presence of a magnetic flux Φ through the section of the hybrid nanowire, the system exhibits the so-called Little-Parks (LP) effect^{16,17}. In the LP effect, the flux causes the superconducting phase in the shell to acquire a quantized winding around the nanowire axis. The winding number n is an integer, also known as *fluxoid* number¹⁸⁻²⁰, that increases in jumps as Φ grows continuously. Winding jumps occur at half-integer multiples of the superconducting flux quantum $\Phi_0 = h/2e^{21-23}$, and are accompa-

nied by a repeated suppression and recovery of the order parameter modulus Δ , forming LP *lobes* associated with each n . The n^{th} lobe is centered around $\Phi = n\Phi_0$, where Δ reaches a local maximum. The LP effect has been demonstrated experimentally in various regimes^{12,24,25}, and has been shown to be accurately described by theory based on the Ginzburg-Landau formalism^{19,20,26-29}.

Furthermore, the superconducting boundary condition imposed by the shell gives rise to a special type of fermionic subgap states through a combination of normal and Andreev reflection at the core/shell interface. These states are hybrid-nanowire *analogs* of the celebrated Caroli-de Gennes-Matricon (CdGM) states in Abrikosov vortex lines of type-II superconductors^{19,30-32}. We call them analogs because both are subgap states within superconducting boundaries, bound to a region with suppressed pairing and threaded by a magnetic flux. However, several important differences exist between them. Some of these were analyzed recently in Ref. 33 and 34, but otherwise this remains a unexplored subject.

In type-II superconductors, CdGM states are low energy excitations bound to the center of each vortex core, i.e, to the region of radius $r \lesssim \xi$ (with ξ the bulk superconducting coherence length)³⁰. Each vortex core is threaded by a single flux quantum (unless the superconductor is sufficiently small³⁵), which produces a localized suppression of the modulus $\Delta(r)$ of the superconducting order parameter as a function of radial coordinate r , see Fig. 1(b), and a winding $n = 1$ of its phase. In full-shell nanowires, on the contrary, the flux is not quantized through the core due to the thinness of the shell

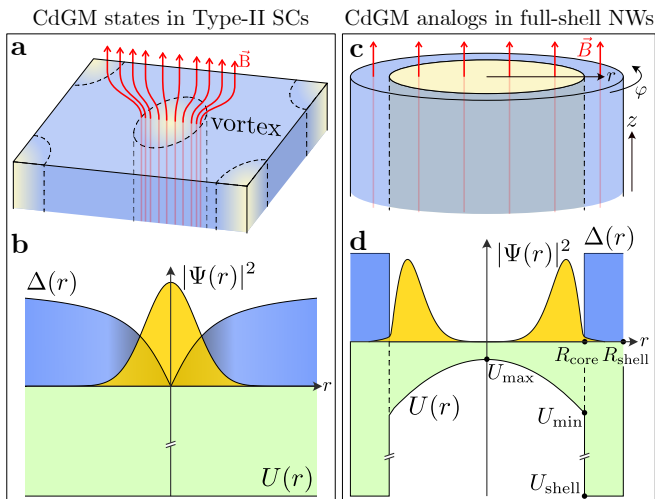


FIG. 1. (a) Schematic of Abrikosov vortex lines in a type-II superconductor. The magnetic flux of the external magnetic field \vec{B} inside each vortex is quantized to the superconducting flux quantum Φ_0 . (b) Pairing potential $\Delta(r)$ (blue), electrostatic potential energy $U(r)$ (green) and lowest-energy CdGM wavefunction density $|\Psi(r)|^2$ (yellow) as a function of radial coordinate r with respect to the vortex center. (c) Schematic of a full-shell hybrid nanowire in a cylindrical approximation. The semiconducting core of radius R_{core} (yellow) is fully covered by an s -wave superconducting shell of thickness $R_{\text{shell}} - R_{\text{core}}$ (blue). The magnetic flux Φ due to the field \vec{B} threading the wire is not quantized and the superconductor gap inside the shell is modulated with Φ following the Little-Parks (LP) effect. (d) Same as (b) but for the full-shell wire. The conduction band bottom inside the semiconductor exhibits a dome-like radial profile with maximum value at the center, U_{max} , and minimum value at the superconductor/semiconductor interface, U_{min} . The electrostatic potential of the metallic shell is $|U_{\text{shell}}| \gg |U_{\text{min}}|$.

and its superconducting gap is modulated with flux into a series of LP lobes, as mentioned earlier. This makes the hybrid wire a multi-fluxoid version of the Abrikosov vortex line. Moreover, the confinement of CdGM states inside the core is dominated by Andreev reflection off the surrounding bulk superconductor, which results in a vanishing group velocity along the vortex line (here the z -direction, see Fig. 1). In contrast to the case of type-II superconductors, in full-shell nanowires the materials of the superconducting shell and the semiconducting core are different. Even though the shell is epitaxially grown with high quality around the core, the unavoidable velocity mismatch between the two materials produces an abrupt decay of $\Delta(r)$ at the interface, see Fig. 1(d), as well as an enhanced normal reflection for electrons in its interior. As a result, CdGM analogs in the core have a large Fermi velocity in the z -direction³³, and form quasi one-dimensional subbands (as opposed to the non-dispersive CdGM states that are confined inside vortices by strong Andreev reflection). Another important consequence of the difference in shell and core materials is

the band alignment due to their work-function difference, which produces a significant semiconductor band bending of the Ohmic-type at the interface³⁶. This band bending, shown as a dome-like profile in Fig. 1(d), creates a quantum well at the core/shell interface and thus an accumulation of charge in that region. Hence, we will see that CdGM analogs are typically localized close to the core/shell interface in the radial direction, unlike the CdGM states in Abrikosov vortices³⁷.

In this work we study the structure and properties of CdGM analogs in realistic full-shell wires, and the information these states can provide about key nanowire aspects through local measurements. We identify the CdGM analogs as Van Hove singularities of the n -dependent, quasi-one dimensional, traverse subbands propagating along the axis of the proximitized nanowire core. We use a cylindrical model for the hybrid wire, although this approximation is not critical to our findings. Subbands are thus characterized by an angular momentum quantum number, m_L , much like the original CdGM states. They are also characterized by a good radial quantum number (for typical nanowire radii only a few, lowest-energy ones are occupied, in contrast to the case of vortex cores in type-II superconductors). We study the CdGM subgap energies and their dispersion with magnetic flux inside each n -lobe. We compute both local density of states (LDOS) calculations at the end of a semi-infinite wire, and differential conductance (dI/dV) through a normal/superconducting junction. The states with $m_L > 0$ ($m_L < 0$) disperse with positive (negative) slope versus Φ , due to a diamagnetic coupling inside the core. In a simplified hollow-core model for the hybrid wire, where all the semiconductor wavefunction is assumed to be confined to a layer of vanishing thickness at the core-shell interface, the CdGM-Van Hove singularities disperse with flux symmetrically with respect to the lobe centers, where they merge into degeneracy points. However, for realistic solid-core wires, characterized by a potential profile like the one in Fig. 1(d), we find that the CdGM-Van Hove dispersion of the different subbands tends to be skewed relative to the center of each LP lobe for $n > 0$. Indeed, subgap states in full-shell wires were recently found experimentally to skew towards higher fields within each lobe¹. We find that the spectrum in general, and the *skewness* in particular, can be explained by the shift of the (typically metastable) degeneracy point within each n sector towards higher $|\Phi|$. The flux displacement of the degeneracy points is a crucial quantity to understand the subgap spectrum of full-shell nanowires. It is directly related to the spatial wavefunction distribution of the CdGM analogs, or more specifically, to their average radius R_{av} inside the core. We perform numerical simulations for Al/InAs full-shell models to show how R_{av} , and hence the CdGM spectrum within each lobe, are affected by the mismatch between the shell (Al) and the core (InAs) materials. The mismatch increases normal reflection at the expense of Andreev processes at the interface³³. Finally, we develop a

simple analytical theory that accurately describes the numerical subgap spectrum, and is able to extract the average wavefunction position R_{av} from the measured CdGM skewness. This provides an indirect but powerful tool to characterize the screened and otherwise inaccessible interior of full-shell devices.

In most of this work we neglect Zeeman and spin-orbit coupling (SOC) inside the semiconductor since they have a minor effect on the CdGM analogs. The Zeeman effect merely produces small splittings in the otherwise spin-degenerate subgap spectrum. The SOC, on the other hand, is of course essential to the existence of a topological phase and the emergence of MBSs. As we will show, however, it leaves the rest of the subgap spectrum essentially unaffected.

This paper is organized as follows. In Sec. II we characterize the bandstructure, LDOS and quantum numbers of the nanowire modes using a simplified, hollow-core approximation to the full-shell nanowire. We show how the proximity effect induced by the shell contact gives rise to Van Hove singularities that become degenerate at special points. In Sec. III we generalize the model to a finite semiconducting layer thickness, called here the tubular-nanowire model, which results in a reduction of the average wavefunction radius of each mode. This leads to a shift of the degeneracy points towards higher fields and the skewness of the CdGM analogs. In Sec. IV we connect to the experimentally relevant model of a solid-core nanowire with a finite band-bending electrostatic profile in the core. We compute the LDOS at one end of the wire and show how it is related to the tunnelling differential conductance of current experiments^{1,3}. In Sec. V we develop an analytical description that allows to extract microscopic system properties from the measured CdGM spectra. In Sec. VI we discuss the effect of adding Zeeman and spin-orbit couplings to our models. Finally, in Sec. VII we briefly discuss the overall differences between CdGM in type-II superconductors and full-shell nanowires.

II. HOLLOW-CORE NANOWIRE

A. Model

Following Ref. 1, we consider a basic model of a cylindrically symmetric full-shell wire that combines (a) the effect of the magnetic flux on the shell superconductor (i.e. the LP effect), (b) the proximity effect on core subbands with well-defined angular momentum, and (c) the effect of the magnetic flux on core subbands. The hybrid wire in cylindrical coordinates (r, φ, z) is oriented with its axis along z and consists of a semiconducting core of effective mass m^* and radius R_{core} , covered by a superconducting shell of outer radius R_{shell} and thickness $d_{\text{shell}} = R_{\text{shell}} - R_{\text{core}}$.

In this section we make a hollow-core approximation, whereby all the electrons in the core are assumed to be lo-

calized at the interface with the superconductor and thus their radial coordinate is fixed to $r = R_{\text{core}}$ (see illustration in Fig. 3). We thus wish to write an effective Hamiltonian for this system, obtained by integrating out the shell degrees of freedom. This introduces a self-energy Σ_{shell} on the hollow core. We neglect non-local self-energy components (a valid approximation for disordered shells¹), so Σ_{shell} depends only on the angle φ around the cylinder axis. In the Nambu basis $\Psi = (\psi_{\uparrow}, \psi_{\downarrow}, \psi_{\downarrow}^{\dagger}, -\psi_{\uparrow}^{\dagger})$, the Bogoliubov–de Gennes (BdG) Hamiltonian for the proximitized nanowire then reads

$$H = \left[\frac{(p_{\varphi} + eA_{\varphi}\tau_z)^2 + p_z^2}{2m^*} - \mu \right] \tau_z + \Sigma_{\text{shell}}(\varphi), \quad (1)$$

where $p_{\varphi} = -\frac{1}{r}i\partial_{\varphi}$, $p_z = -i\partial_z$ are the momentum operators of electrons (we use $\hbar = 1$ throughout), μ is the semiconductor chemical potential, $e > 0$ is the charge unit and τ_i are the Pauli matrices for the electron/hole degree of freedom. The nanowire is subject to a magnetic field along its axis, $\vec{B} = B_z \hat{z}$. In the symmetric gauge for the vector potential, $\vec{A} = \frac{1}{2}(\vec{B} \times \vec{r})$, one has $\vec{A} = (-y, x, 0)B_z/2 = A_{\varphi}\hat{\varphi}$, where $A_{\varphi} = Br/2$. Note that both A_{φ} and p_{φ} should be evaluated on the hollow-core surface at $r = R_{\text{core}}$.

1. Little-Parks effect

In multiply connected superconductors, such as a ring or a hollow cylinder, and in the presence of an axial magnetic field, the *fluxoid* Φ' is quantized in units of Φ_0 , the superconducting flux quantum^{19,20}. This was established by F. London¹⁸, who defined the fluxoid as the sum of the magnetic flux Φ and an extra term involving the circulation of persistent supercurrents that arise in response to the magnetic flux. In thick-walled superconducting cylinders where the wall thickness is much greater than the London penetration depth^{38,39}, λ_L , or equivalently in vortices inside bulk superconductors, the persistent supercurrent term vanishes deep inside the superconductor, and thus the magnetic flux is also quantized at large distances, $\Phi = \Phi'$. However, in thin-walled superconducting shells as the ones considered here, the Meissner^{40,41} expulsion of the magnetic flux is negligible and thus the magnetic field in the superconductor, as well as in its interior, is essentially the same as the applied one (and is hence not quantized). In this case, the second term involving the screening supercurrents oscillates with flux as the fluxoid increases in units of Φ_0 , which in turn produces a modulation of the critical temperature T_c with a period Φ_0 . This is known as the LP effect^{16,17,42,43}. From a complementary point of view, the modulation of T_c with flux or, equivalently, of the cylinder superconducting gap Δ , is a consequence of the pair breaking effect of the threading magnetic flux over the Cooper pairs in the superconductor. This pair-breaking effect is minimal at integer values of Φ/Φ_0 , where Δ reaches its

maximum, and maximum at half-integer values, where the fluxoid performs abrupt, first order transitions, and Δ acquires its minimum value (which can even reach zero in the destructive LP regime), see Fig. 2.

Alternatively to the London theory, the quantization of the fluxoid can also be established within the Ginzburg-Landau formalism^{26,44} for the complex superconducting order parameter Δ_φ . Since this is a single-valued quantity, the order parameter phase φ must change by an integer multiple of 2π , $n \in \mathbb{Z}$, when completing a closed path around the cylinder. This winding number is the fluxoid $n = \Phi'/\Phi_0$. One can thus write

$$\Delta_\varphi = \Delta e^{in\varphi}. \quad (2)$$

In the above equation and throughout this work, Δ and n denote the flux-dependent, LP gap and fluxoid number in the shell, respectively, corresponding to a thin shell superconductor, $d_{\text{shell}} \ll \lambda_L$. Their dependence with magnetic flux Φ is implicit unless otherwise specified. The actual $\Delta(\Phi)$ and $n(\Phi)$ are obtained by solving the following set of equations^{25,28,29,45-47}

$$\begin{aligned} n(\Phi) &= [\Phi/\Phi_0] = 0, \pm 1, \pm 2, \dots, \\ \ln \frac{T_c(\Phi)}{T_c(0)} &= \mathcal{D}\left(\frac{1}{2}\right) - \mathcal{D}\left(\frac{1}{2} + \frac{\Lambda(\Phi)}{2\pi k_B T_c(\Phi)}\right), \\ \Lambda(\Phi) &= \frac{\xi^2 T_c(0)}{\pi R_{\text{LP}}^2} \left[4 \left(n - \frac{\Phi}{\Phi_0} \right)^2 + \frac{d_{\text{shell}}^2}{R_{\text{LP}}^2} \left(\frac{\Phi^2}{\Phi_0^2} + \frac{n^2}{3} \right) \right], \\ \frac{\Delta(\Phi)}{\Delta(0)} &\approx \left(\frac{T_c(\Phi)}{T_c(0)} \right)^{3/2}. \end{aligned} \quad (3)$$

Here \mathcal{D} denotes the digamma function, Λ is the pair-breaking parameter^{45,48} and ξ is zero-field superconducting coherence length. The total flux is defined as

$$\Phi = \pi R_{\text{LP}}^2 B_z, \quad (4)$$

where

$$R_{\text{LP}} \approx \frac{R_{\text{core}} + R_{\text{shell}}}{2} \quad (5)$$

is approximately equal to the mean radius of the shell¹.

The solution for the transcendental Eqs. (3) is qualitatively different depending on the ratios R_{LP}/ξ and $d_{\text{shell}}/R_{\text{LP}}$. It ranges from the non-destructive regime (Δ is non-zero, satisfied for $R_{\text{LP}}/\xi \gtrsim 0.6$ if $d_{\text{shell}} \rightarrow 0$) to the destructive regime (Δ vanishes in a finite window around odd half-integer Φ/Φ_0 , satisfied for smaller R_{LP}/ξ). The different regimes are represented in Fig. 2, solid lines. As a guideline, some typical values representative of recent experiments¹² are $\xi \sim 100$ nm, $R_{\text{core}} \sim 70$ nm, $d_{\text{shell}} \sim 10$ nm and $\lambda_L = 150$ nm. These parameters correspond to a superconductor in the dirty limit, which is the realistic regime in current experiments.

A much simpler, approximate parametrization of the LP solution for $\Delta(\Phi)$ can be obtained^{24,49} in terms of the

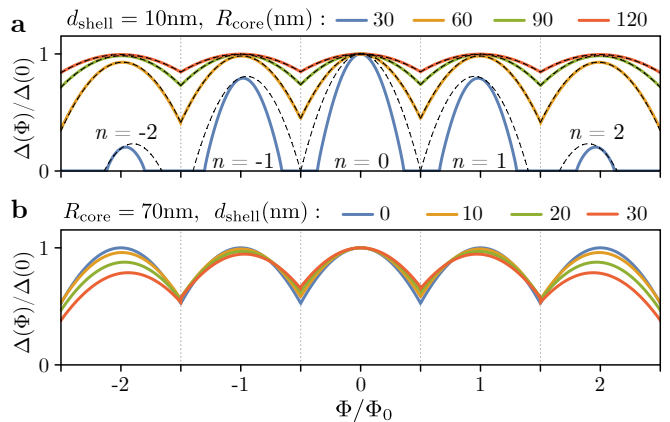


FIG. 2. (a) Little-Parks (LP) variation of the shell gap $\Delta = |\Delta_\varphi|$ with applied axial flux (normalized to the superconducting flux quantum Φ_0) of a superconducting cylindrical shell of thickness d_{shell} , $\xi = 80$ nm and various internal radii R_{core} . $n = 0, \pm 1, \pm 2$ label the different LP lobes. Solid lines correspond to the Ginzburg-Landau solution, and dashed lines to the approximation of Eq. (6) (b) Same as (a) but for fixed internal shell radius R_{core} and varying d_{shell} .

ratios $\delta_{1/2} \equiv \Delta(\frac{1}{2}\Phi_0)/\Delta(0)$ and $\delta_2 \equiv \Delta(2\Phi_0)/\Delta(0)$, instead of R_{LP}/ξ and $d_{\text{shell}}/R_{\text{LP}}$,

$$\begin{aligned} n &= [\Phi/\Phi_0] = 0, \pm 1, \pm 2, \dots, \\ \frac{\Delta(\Phi)}{\Delta(0)} &= \left[1 - c_1 \left(\frac{\Phi}{\Phi_0} - n \right)^2 - c_2 \frac{\Phi^2}{\Phi_0^2} \right], \\ c_1 &\equiv \frac{15 + \delta_2 - 16\delta_{1/2}}{4}, \\ c_2 &\equiv \frac{1 - \delta_2}{4}. \end{aligned} \quad (6)$$

This approximation, shown in dashed lines in Fig. 3(a), is accurate in the non-destructive regime and slightly deviates in the destructive one. We will use it in the former scenario, which will be the main case of interest throughout the remainder of this work. Our results are nevertheless trivially generalized to the LP destructive regime, see for instance Fig. 6, where we will make use of the exact equations.

2. Self-energies Σ_{shell}^0 and $\Sigma_{\text{shell}}^\infty$

The concrete form of the self-energy $\Sigma_{\text{shell}}(\varphi)$ in Eq. (1) admits several levels of approximation. We assume the shell to have a superconducting pairing potential $\Delta_\varphi = \Delta e^{in\varphi}$ as discussed above. In its simplest possible version, the self-energy is frequency independent, and equal to the induced pairing, which in the Nambu basis takes the form

$$\Sigma_{\text{shell}}^0(\varphi) = \Delta^* \tau_{n\varphi}, \quad (7)$$

where we denote

$$\tau_{n\varphi} = \tau_x \cos n\varphi + \tau_y \sin n\varphi. \quad (8)$$

The modulus Δ^* of the (flux-independent) induced pairing is proportional to the zero-flux parent $\Delta(0)$,

$$\Delta^* = \tau^* \Delta(0). \quad (9)$$

Here, $\tau^* \in [0, 1]$ is a dimensionless coefficient related to the shell/core transparency, and which represents the strength of the proximity effect.

The Σ_{shell}^0 self-energy is a reasonable approximation only for energies/frequencies much smaller than the shell gap Δ (large gap approximation). A more precise, yet still simple form of Σ_{shell} can be derived by considering the shell at a given φ as an unbounded superconducting metal with energy-independent normal density of states. Integrating it out gives an ω -dependent self-energy

$$\Sigma_{\text{shell}}^\infty(\varphi) = \Gamma_N \frac{\omega\tau_z - \Delta(\Phi)\tau_{n\varphi}}{\sqrt{\Delta(\Phi)^2 - \omega^2}}, \quad (10)$$

$$\Gamma_N = \Delta^* \sqrt{\frac{1 + \tau^*}{1 - \tau^*}}. \quad (11)$$

The above expression for the normal decay rate Γ_N is derived in Sec. V. This $\Sigma_{\text{shell}}^\infty$ self-energy model is commonly used^{4,50,51} and correctly yields important qualitative features of the subgap spectrum of hybrid systems, such as the repulsion between subgap levels and the BCS singularity at the gap edge. It satisfies $\Sigma_{\text{shell}}^0 = \lim_{\Delta \rightarrow \infty} \Sigma_{\text{shell}}^\infty$ at constant Δ^* and ω . Note that $\Sigma_{\text{shell}}^\infty$ makes the effective Hamiltonian ω -dependent, so that it must be actually understood as the inverse of the core Green's function $G(\omega) = [\omega - H(\omega)]^{-1}$, from which spectral densities and other observables can be computed.

In later sections we will present a third, more sophisticated self-energy $\Sigma_{\text{shell}}^{1D}$ that is more accurate and better motivated microscopically.

3. Quantum numbers

The hollow-core model in Eq. 1 exhibits three symmetries that can be used to classify its eigenstates¹. First, H commutes with electron spin along any direction, so its projection $s_z = \pm \frac{1}{2}$ along z in particular is a good quantum number. Second, the nanowire is assumed, for the moment, to be infinite, so translation symmetry along z leads to a good k_z quantum number. Third, the Hamiltonian exhibits cylindrical symmetry, generalized to account for the winding of Δ_φ . The generalized angular momentum $L_z = -i\partial_\varphi + \frac{1}{2}n\tau_z$ commutes with H , $[L_z, H] = 0$, so that the eigenvalues m_L of L_z are also good quantum numbers of the eigenstates of H . The possible eigenvalues m_L of L_z are⁵²

$$m_L = \begin{cases} \mathbb{Z} & \text{if } n \text{ is even} \\ \mathbb{Z} + \frac{1}{2} & \text{if } n \text{ is odd} \end{cases}, \quad (12)$$

which points to qualitative differences between the spectrum in even and odd LP lobes. The canonical transformation $U = e^{-i(m_L - \frac{1}{2}n\tau_z)\varphi - ik_z z}$ then reduces H to

a φ -independent 4×4 BdG effective Hamiltonian $\tilde{H} = U H U^\dagger$, where

$$\tilde{H} = \left[\frac{(m_L - \frac{1}{2}n\tau_z + \frac{1}{2}\frac{\Phi}{\Phi_0}\tau_z)^2}{2m^*R_{\text{core}}^2} + \frac{k_z^2}{2m^*} - \mu \right] \tau_z + \Sigma_{\text{shell}}(0). \quad (13)$$

The eigenstates $\tilde{\Psi}_{m_L, k_z, s_z}$ of \tilde{H} are related to the original eigenstates $\Psi_{m_L, k_z, s_z}(\varphi, z)$ of H by $\Psi_{m_L, k_z, s_z}(\varphi, z) = U^\dagger(\varphi, z)\tilde{\Psi}_{m_L, k_z, s_z}$.

In absence of proximity effect (i.e., for $\Delta^* = 0$), the decoupled (normal) core Hamiltonian commutes with the conventional angular momentum $l_z = -i\partial_\varphi$, so that its eigenstates can be classified in terms of the integer eigenvalues of l_z , denoted by m_l ,

$$m_l = \mathbb{Z}, \quad (14)$$

together with k_z and s_z . In the normal case, then, the canonical transformation that diagonalizes the Hamiltonian is simply $U = e^{-im_l\varphi - ik_z z}$.

B. Van Hove singularities and degeneracy points

We are now ready to analyze the Nambu band structure of the hollow-core nanowire model. We do so in two different configurations: $\Delta^* = 0$ (isolated core) and $\Delta^* > 0$ (proximitized core). The results, for four different values of the flux (two in the $n = 0$ lobe and two in the $n = 1$ lobe), are shown in the different panels of Fig. 3. Thin lines are for $\Delta^* = 0$ Nambu subbands [i.e. normal electron (solid) and hole (dashed) bands], and are coloured according to their corresponding m_l quantum number. Thick lines correspond to finite Δ^* , and are labeled by the corresponding m_L quantum number.

The key feature to note in the finite Δ^* bands is the appearance of avoided crossings between normal electron and hole subbands with m_l differing by the fluxoid number n . The avoided crossings are due to Andreev reflection at the shell/core interface, and result in Van Hove singularities (black dots) in the LDOS that move with magnetic flux. These Van Hove singularities are the full-shell analogs of CdGM states in type-II superconductors (see Sec. VII for further discussion on the connection).

The energies of the Van Hove singularities for different m_L 's become degenerate at certain values of magnetic flux, see Figs. 3(a,d). These special values of flux correspond to integer multiples of Φ_0 when flux is computed as $\Phi = \pi R_{\text{core}}^2$. In the limit of thin shells, we have $R_{\text{LP}} = R_{\text{core}}$, so this coincides with Eq. (4), defined in the context of the Little-Parks effect. Thus, for thin shells and hollow cores, the proximity-induced Van Hove singularities become degenerate at the center of each lobe.

C. Local density of states

The Van Hove singularities and their degeneracies can also be visualized in terms of the LDOS at the end of a

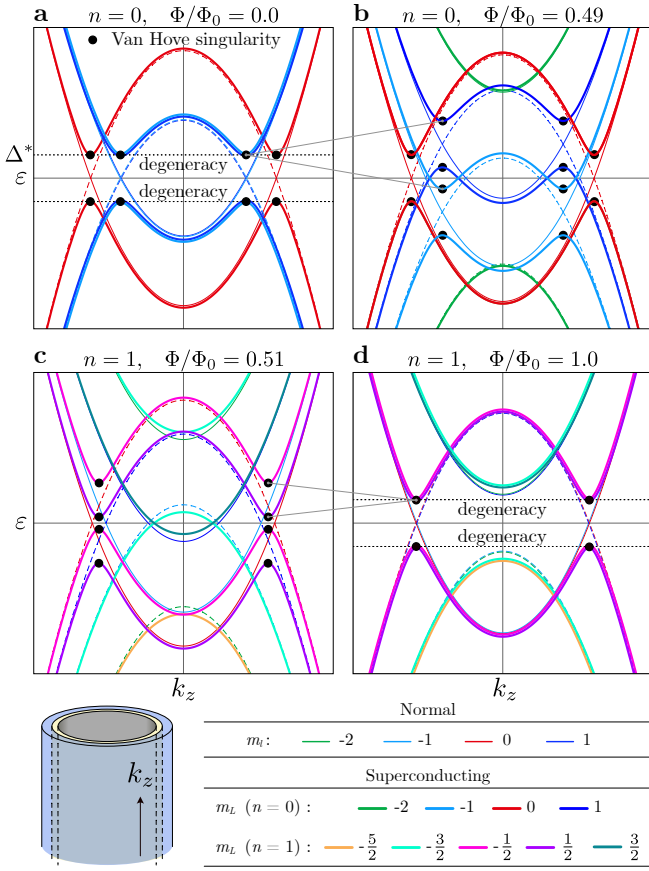


FIG. 3. (a) Bogoliubov-de Gennes bandstructure of an infinite $r = R_{\text{core}}$ hollow-core nanowire vs longitudinal momentum k_z at the center of the $n = 0$ LP lobe (zero flux). Thin solid (dashed) lines correspond to the normal electron (hole) bands, with $\Delta^* = 0$, whereas thick lines correspond to the superconducting state, with $\Delta^* \neq 0$. Different colors signal different (generalized) angular momentum number m_l (m_L) for the normal (superconducting) subbands. Both m_l and m_L are integers in the $n = 0$ lobe, see legend. The superconducting pairing turns finite-momentum electron-hole crossings with equal m_L into anticrossings, with Van Hove singularities arising at the edges of the corresponding gaps, see black dots. In the absence of applied flux, $\Phi = 0$, all anticrossings are equal in magnitude and centered at zero energy, so that all Van Hove singularities become degenerate. (b) Same as (a) but for a flux close to the edge of the $n = 0$ lobe, $\Phi/\Phi_0 = 0.49$. Previously degenerate Van Hove singularities split in energy due to the different dispersion with flux of electron and hole m_L subbands. (c) Same as (b) but for a flux close to the lower edge of the $n = 1$ lobe. The normal bands are very similar to (b), but the anticrossing pattern has changed, as the pairing only couples electron and holes with m_L differing by n . The superconducting subband colors correspond to half-integer m_L angular-momentum quantum numbers. (d) Same as (c) but at the center of the $n = 1$ lobe where the hollow core is threaded by one flux quantum. The van Hove singularity degeneracies of different subbands are recovered.

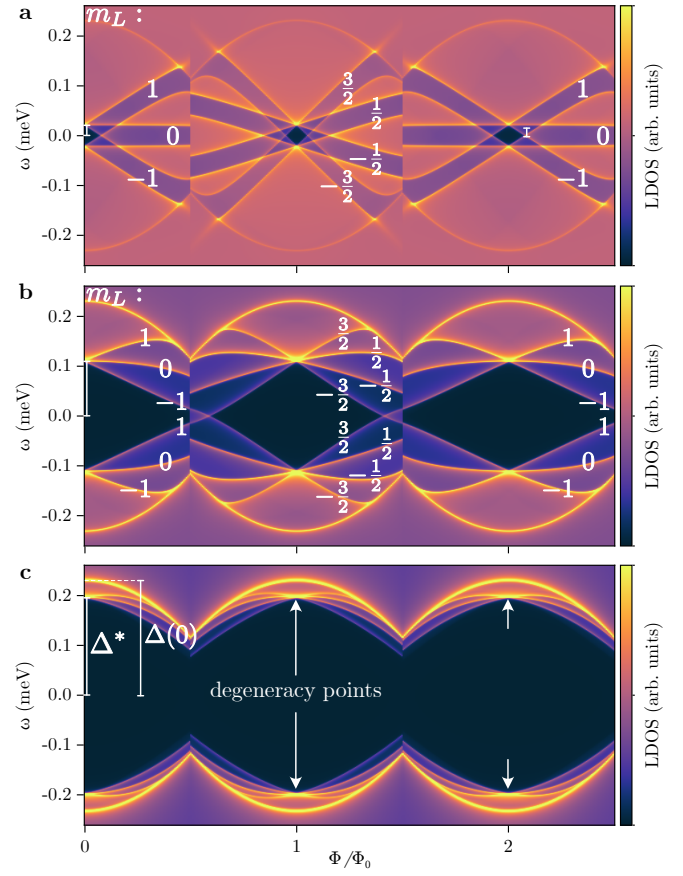


FIG. 4. (a) Local density of states (LDOS) at the end of a semi-infinite hollow-core nanowire (in arbitrary units) vs energy, ω , and applied normalized flux, Φ/Φ_0 , displaying half of the zeroth lobe, first and second lobes. CdGM analogs are shown as subgap features below the LP parent gap $\Delta(\Phi)$, together with their generalized angular momentum m_L . From top to bottom: weak superconductor/semiconductor coupling, $\Gamma_N = 0.1\Delta(0)$ (a), intermediate coupling, $\Gamma_N = 0.8\Delta(0)$ (b) and strong coupling, $\Gamma_N = 3\Delta(0)$ (c). Degeneracy points (where all CdGM Van Hoves cross) happen at the center of each lobe (where the normalized flux Φ/Φ_0 is an integer), see arrows in (c). The lowest subgap level at zero flux is dubbed the induced gap Δ^* . Parameters: $R_{\text{axis}} = R_{\text{core}} = R_{\text{shell}} = 70$ nm, $\Delta(0) = 0.23$ meV, $\mu = 1$ meV, $c_1 = 2$, $c_2 = 0$, $m^* = 0.026 m_e$ and $a_0 = 5$ nm.

semi-infinite hollow-core nanowire. The LDOS is given by

$$\rho(\omega) = -\frac{1}{\pi} \sum_{m_L} \text{Im} G_{m_L}^0(\omega), \quad (15)$$

where the retarded Green function $G_{m_L}^0(\omega)$ may be computed by discretizing the rotated Hamiltonian \tilde{H} in a one-dimensional lattice along z , with lattice constant a_0 , and using standard methods of scattering theory⁵³ to obtain $G_{m_L}^0(\omega)$ in the first unit cell. The superindex 0 here stands for the first site of the semi-infinite chain.

In Fig. 4 we show the resulting LDOS $\rho(\omega)$ as a func-

tion of energy ω and normalized flux Φ/Φ_0 , for different values of core/shell coupling Γ_N , and thus of induced gap Δ^* . For this computation we have used the self-energy $\Sigma_{\text{shell}}^\infty$, which introduces a visible BCS singularity from the parent superconductor at $\Delta(\Phi)$. We have focused on the non-destructive LP regime with $d_{\text{shell}} \approx 0$, so that all lobes have an identical shape.

The (spin-degenerate) Van Hove singularities, visible as sharp, flux-dependent subgap features in each lobe, are labeled with their corresponding m_L . Note that each CdGM analog consists of both the bright Van Hove singularity itself (in orange color in Fig. 4) and a tail extending above or below it till the band edge. It is important to note that only the shell-induced Van Hove singularities (dots in Fig. 3) appearing at finite momentum k_z have a good visibility in the LDOS. In contrast, $k_z = 0$ Van Hoves, as those already present in the normal bands, are essentially invisible in LDOS due to the vanishing slope of their electron wave function at the end of the nanowire^{54,55}

The number of singularities is different in even and odd lobes. Since m_L is integer in even lobes, these contain an odd number of Van Hoves $\pm\omega$ pairs for a given flux. Odd lobes, in contrast, have half-integer m_L , so they contain always an even number of Van Hove pairs. Van Hoves converge at the center of each lobe, coalescing in a characteristic fountain-like pattern at degeneracy points, both for positive and negative ω . The slope with Φ of each Van Hove in this fountain is proportional to m_L . This is ultimately due to the diamagnetic coupling

$$\sim \frac{1}{2m^*R_{\text{core}}^2} \frac{\Phi}{\Phi_0} m_L \tau_z = \omega_{\mathcal{L}} m_L \tau_z, \quad (16)$$

that is produced in Eq. (13) by expanding the square. Here, $\omega_{\mathcal{L}} = eB_z/2m^*$ is the Larmor frequency³¹. The slope is not constant, however, since the BCS singularity at energy $\Delta(\Phi)$ in $\Sigma_{\text{core}}^\infty$ deforms the Van Hove fountain as it approaches the gap edge, particularly as Δ^* approaches the parent $\Delta(0)$.

III. TUBULAR-CORE NANOWIRE

To continue building towards the realistic nanowire modes in Sec. IV, we will now generalize the hollow-core model by giving a finite thickness $d_{\text{core}} = R_{\text{core}} - R_{\text{axis}}$ to the semiconductor, so that it spans a finite range of radii $r \in [R_{\text{axis}}, R_{\text{core}}]$, see Fig. 5(a). We dub this the tubular-core nanowire model.

A. Model

The tubular generalization introduces radial kinetic energy into the model, and consequently radially quan-

tized modes. The BdG effective Hamiltonian reads

$$H = \left[\frac{(p_\varphi + eA_\varphi(r)\tau_z)^2 + p_r^2 + p_z^2}{2m^*} - \mu \right] \tau_z + \Sigma_{\text{shell}}(\varphi), \quad (17)$$

where $p_r^2 = -\frac{1}{r}\partial_r(r\partial_r)$. Note that we have also restored the radial dependence into $A_\varphi(r) = B_z r/2$. The same canonical transformation U reduces the above to

$$\tilde{H} = \left[\frac{(m_L - \frac{1}{2}n\tau_z + \frac{1}{2}\frac{\Phi}{\Phi_0}\tau_z)^2}{2m^*r^2} + \frac{k_z^2 + p_r^2}{2m^*} - \mu \right] \tau_z + \Sigma_{\text{shell}}(0). \quad (18)$$

To find the eigenstates $\tilde{\Psi}(r)$ of \tilde{H} we follow the DLL-FDM scheme of Ref. 56. We first discretize the radial coordinate r with a lattice spacing a_0 , replacing derivatives with finite differences in the differential eigenvalue equation $\tilde{H}\psi(r) = \varepsilon\tilde{\Psi}(r)$. We then absorb the Jacobian $J = r$ of the cylindrical coordinates into modified discrete eigenstates $F(r_i) = \tilde{\Psi}(r_i)\sqrt{r_i}$ and into the corresponding Hamiltonian $H' = r^{1/2}\tilde{H}r^{-1/2}$. We arrive at a discrete eigenvalue problem $\sum_{i'} H'_{ii'} F(r_{i'}) = \varepsilon F(r_i)$ with a Hermitian Hamiltonian matrix $H'_{ii'}$, whose discrete eigenstates are, by virtue of their definition, trivially orthonormal without J , $\sum_i F_\alpha^*(r_i)F_\beta(r_i) = \delta_{\alpha\beta}$. The kinetic energy $\tau_z p_r^2/m$ transforms in $H'_{ii'}$ into an onsite term $o_i = 2t_0\tau_z$ plus a radial hopping $t_{ii'} = -t_0\tau_z r/\sqrt{r_i r_{i'}}$ between the nearest neighbors, where $t_0 = 1/(2m^*a_0^2)$. Note that the $r/\sqrt{r_i r_{i'}}$ factor directly stems from the cylindrical Jacobian, but does not break the symmetry $t_{ii'} = t_{i'i}$. Also, when applying the above DLL-FDM scheme to systems including the origin $r = 0$, the correct boundary condition must be implemented there. This is done by excluding the $r = 0$ site and multiplying o_i at the $r = a_0$ site by $3/4$.⁵⁶

1. Improved self-energy $\Sigma_{\text{shell}}^{1D}$

A $\Sigma_{\text{shell}}^\infty$ self-energy could be used to good effect in the tubular nanowire model \tilde{H} above by applying it locally on sites at $r = R_{\text{core}}$. In this section, however, we wish to introduce an improved self-energy model that captures the coupling of different m_l modes to the shell more precisely. The actual couplings depend not only on the amplitude of the modes at $r = R_{\text{core}}$, but on their velocity at either side of the interface. The different materials in the core and shell impose a mode-dependent velocity mismatch, not captured by $\Sigma_{\text{shell}}^\infty$, that reduces the maximum transparency possible for a given mode.

The improved expression for Σ_{shell} presented below is similar to the one employed in the theory of Ref. 1. We model the shell at $r > R_{\text{core}}$ as a set of decoupled, semi-infinite, one-dimensional (1D), superconducting chains, with pairing $\Delta(\Phi)\tau_x$ (the φ dependence already transformed away by U), Fermi energy μ_S and effective mass m_S^* of Al. These chains require a much finer discretization $a_S = 0.01$ nm to accurately describe the

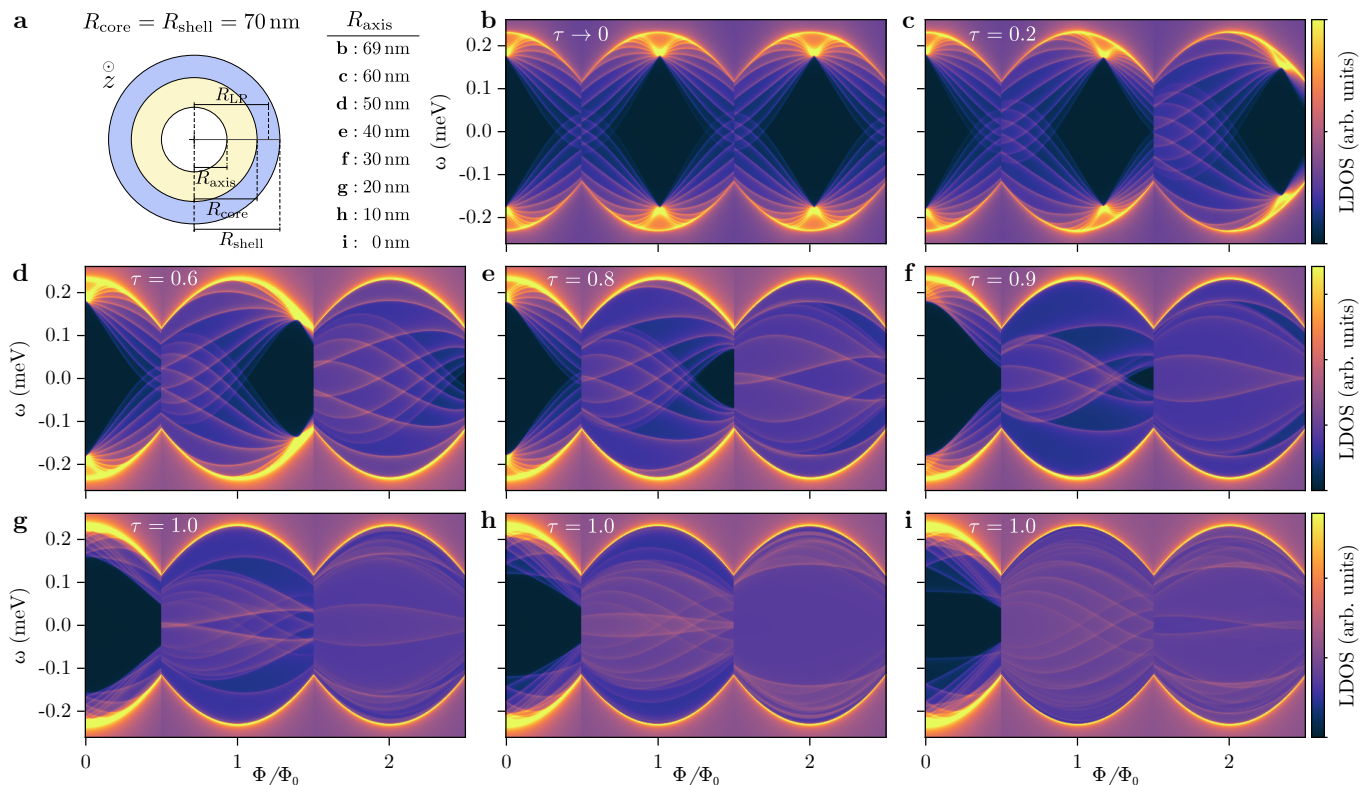


FIG. 5. (a) Schematics of the full-shell nanowire cross section for a semiconducting tubular core with R_{axis} inner and R_{core} outer radii. The outer shell radius is R_{shell} . (b-i) LDOS in arbitrary units vs energy and normalized flux for increasing tubular-core thickness $d_{\text{core}} = R_{\text{core}} - R_{\text{axis}}$, from the hollow-core approximation in (a) to the solid-core case in (i). The corresponding values of R_{axis} are displayed in (a). The uniform electrostatic potential inside the semiconductor is adjusted in each panel to have 12 (spin-degenerate) m_L subbands occupied at zero flux. The dimensionless superconductor/semiconductor coupling τ is adjusted to keep $\Delta^* \approx 0.8\Delta(0)$, with its value indicated in each panel. The core lattice constant a_0 is adjusted to have $N \gtrsim 11$ discretization points in the radial direction [ranging from $a_0 = 0.1$ nm in (b) to $a_0 = 5$ nm in (i)]. Other parameters: $R_{\text{core}} = R_{\text{shell}} = 70$ nm, $\Delta(0) = 0.23$ nm, $c_1 = 2$, $c_2 = 0$, $a_S = 0.01$ nm and $V_S = -11$ eV.

small Fermi wavelength of Al, and a consequently larger $t_s = 1/(2m_S a_S^2)$. Using the same method of Sec. II C we can compute the Green's function $G_{\text{shell}}^0(\omega)$ on the first site of each chain.

The above shows how to discretize the core and shell regions separately, but does not specify how to discretize the system across the interface, where both the effective mass and lattice spacing change. To do so, we must generalize the scheme above, using a radial kinetic energy that is adequately symmetrized with a position dependent mass $m(r)$, as $-\frac{1}{2r}\partial_r[\frac{r}{m(r)}\partial_r]$, prior to its discretization⁵⁶. We generalize the definition of eigenstates $F(r_i)$ to account for the inhomogeneous mesh, so that they remain trivially orthonormal. This is achieved by incorporating both the Jacobian and discretized differential dr as shown in Ref. 57, $F(r_i) = \Psi(r_i)\sqrt{r_i(r_{i+1} - r_{i-1})/2}$. We arrive at a general discretized form for the kinetic energy, given by a nearest-neighbour hopping amplitude between any two sites i and $i' = i + 1$ at r_i and $r_{i'}$ (possibly at

different sides of the interface) of the form

$$t_{ii'} = t_{i'i} = -\tau_z \frac{1}{m(\bar{r})a\sqrt{(r_{i'} - r_{i-1})(r_{i+1} - r_i)}} \frac{\bar{r}}{\sqrt{r_i r_{i'}}}. \quad (19)$$

Here $\bar{r} = (r_i + r_{i'})/2$ is the average position and $a = r_{i'} - r_i$ is the distance between the two sites. When both sites are inside the shell, the last Jacobian factor $\bar{r}/\sqrt{r_i r_{i'}}$ is dropped, so $t_{ii'} = -t_S \tau_z$ as discussed above. The additional onsite energy contribution of the kinetic energy reads

$$o_i = \tau_z \frac{1}{r_{i+1} - r_{i-1}} \left[\frac{r_{i+1/2}}{(r_{i+1} - r_i)m(r_{i+1/2})} + \frac{r_{i-1/2}}{(r_i - r_{i-1})m(r_{i-1/2})} \right], \quad (20)$$

where $r_{i\pm 1/2} = (r_i + r_{i\pm 1})/2$.

Given the dependence of $t_{ii'}$ on next-nearest parameters, integrating out the 1D shell chains is optimally done by incorporating the first site of the chain (denoted by index $i = N_S$) into the core, and integrating from the second site $N_S + 1$ onward, for which the tight-binding

Hamiltonian is periodic, with hopping $t_{ii'} = -t_S \tau_z$ and onsite energy $o_i = (2t_S - \mu_S) \tau_z - \Delta \tau_x$. Denoting the hopping $t_I = t_{N_S, N_S+1} = -1/(2m_S a_S \sqrt{a_S(a_S + a_0)/2})$, we can then write the shell-induced self-energy on site N_S as

$$\Sigma_{\text{shell}}^{1D}(\omega) = \tau t_I^2 G_{\text{shell}}^0(\omega). \quad (21)$$

Here, we have introduced a dimensionless parameter $\tau \in [0, 1]$ that should not be confused with τ^* in Eq. (9), but which plays a similar role of modelling a non-perfect core/shell interface transparency. A value $\tau = 0$ represents a core decoupled from the shell, with perfect normal reflection of core modes at the interface, while $\tau = 1$ models a maximal core/shell transparency, with the highest Andreev reflection probability allowed by the velocity mismatch between core and shell. The induced gap Δ^* in this model depends on the specific m_L mode. Each mode will generally have a slightly different wavefunction profile, and hence a different amplitude and velocity at the interface, both crucial to determine its relative Andreev vs normal reflection probability.

B. Degeneracy point shifts and skewness

The evolution of the subgap Van Hove singularities as we go from the hollow-core to the tubular-core nanowire of decreasing R_{axis} is shown in Fig. 5, all the way to $R_{\text{axis}} = 0$. Note that for the moment the electrostatic potential across the tubular core is kept uniform for simplicity. The most immediate effect of gradually reducing R_{axis} is a shift of the degeneracy point (originally located at the center of each LP lobe in the hollow-core nanowire) towards higher fields for $n > 0$, see e.g. Fig. 5(b) vs Fig. 5(c). The shift can make the degeneracy point exit the $n > 0$ lobe altogether as in Figs. 5(e-i). In the process, the fountain-like set of CdGM Van Hove singularities progressively fill the $n > 0$ lobes as the “tent”-shaped gap below the degeneracy point also gets shifted to the right for $n > 0$, eventually also disappearing, Fig. 5(g). As a result, the CdGM Van Hove singularities appear as subgap features skewed towards higher fields relative to the center of the LP lobes, see Figs. 5(d-f). For sufficiently small R_{axis} , however, the skewness becomes inverted, see Figs. 5(f-i). This inversion happens sooner at higher LP lobes. The skewness of CdGM analogs is thus found to be a direct consequence of the shift of the core degeneracy points, which becomes the central concept to understand the tubular-core nanowire.

The shift of degeneracy points can be readily understood in terms of the wavefunction distribution of modes in the core. In the hollow-core model we showed that degeneracy points appeared at integer normalized flux, as experienced by core states. The fact that this condition matched the integer normalized flux as experienced by the shell (center of LP lobes) was a consequence of the simplifying assumption that $R_{\text{core}} = R_{\text{shell}} = R_{\text{LP}}$, since then the area spanned by the superconductor and

core states coincided. Now, in the tubular-core model, as the core wavefunctions are allowed to spread inwards throughout the interval $r \in [R_{\text{axis}}, R_{\text{core}}]$, see Fig. 6(e), the flux they experience at a given magnetic field is decreased respect to the LP flux Φ into the shell. This shifts the degeneracy points towards higher magnetic fields.

The shift can be quantified by considering that the flux experienced by the spread-out wavefunction is the same as if it were concentrated at its average radius $R_{\text{av}} = \langle r \rangle$. (Figure 6(e) shows that, since the electrostatic potential is uniform, $R_{\text{av}} \approx (R_{\text{axis}} + R_{\text{core}})/2$ for all m_l modes if $R_{\text{axis}}/R_{\text{core}} \gtrsim 0.5$.) The flux at which the degeneracy point happens, $\Phi_{\text{dp}} = \pi R_{\text{LP}}^2 B_z^{\text{dp}}$, then becomes

$$\Phi_{\text{dp}}/\Phi_0 = (1 + \delta n_{\text{dp}})n = \frac{R_{\text{LP}}^2}{R_{\text{av}}^2}. \quad (22)$$

Taking Fig. 5(d) as a starting point, we show in Fig. 6(a-d) the change in dimensionless shift δn_{dp} when adjusting $R_{\text{LP}}/R_{\text{av}}$. For clarity, we have first fixed in Fig. 6(a,b) the shell gap $\Delta(\Phi)$ to a constant $\Delta(0) = 0.23$ meV, so that the LP modulation does not obscure the degeneracy point shift [the corresponding LDOS with the correct $\Delta(\Phi)$ is shown in panels Fig. 6(c,d)]. It is clear from Eq. (22) that if $R_{\text{av}} < \sqrt{2/3}R_{\text{LP}}$, then $\delta n_{\text{dp}} > 1/2$ and thus we move the $n = 1$ degeneracy point out of the $n = 1$ LP lobe. This is shown in Fig. 6(b), where R_{LP} is increased by setting $R_{\text{shell}} = 90$ nm. In this situation, the $n = 1$ degeneracy point does not correspond any more to a stable configuration for any value of magnetic field, since the fluxoid number in the ground state changes from $n = 1$ to $n = 2$ already at $\Phi/\Phi_0 = 3/2 < 1 + \delta n_{\text{dp}}$. It is rather a metastable configuration in the $n > 1$ LP lobe. We represent this metastable branch inside the dashed white square of Fig. 6(b). Note, however, that the $n = 1$ CdGM skewness does not depend on whether the degeneracy point is a stable or metastable configuration.

IV. SOLID-CORE NANOWIRE

A. Model

We finally study in this section a nanowire model that can be considered a reasonable approximation to the actual full-shell nanowires in recent experiments. These are all solid-core nanowires, i.e., with $R_{\text{axis}} = 0$. We will still consider a cylindrical approximation, since we have found a hexagonal (or otherwise non-axially symmetric) wire’s cross-section to be unimportant in regards to the skewness and overall properties of the CdGM analogs (not shown here). We will include, however, an extra ingredient in the solid-core model that is found to be crucial: the non-homogeneous electrostatic potential $U(r)$ inside the core. This potential is a consequence of the band-bending imposed by the epitaxial core/shell Ohmic contact, which in turn stems from the difference of the

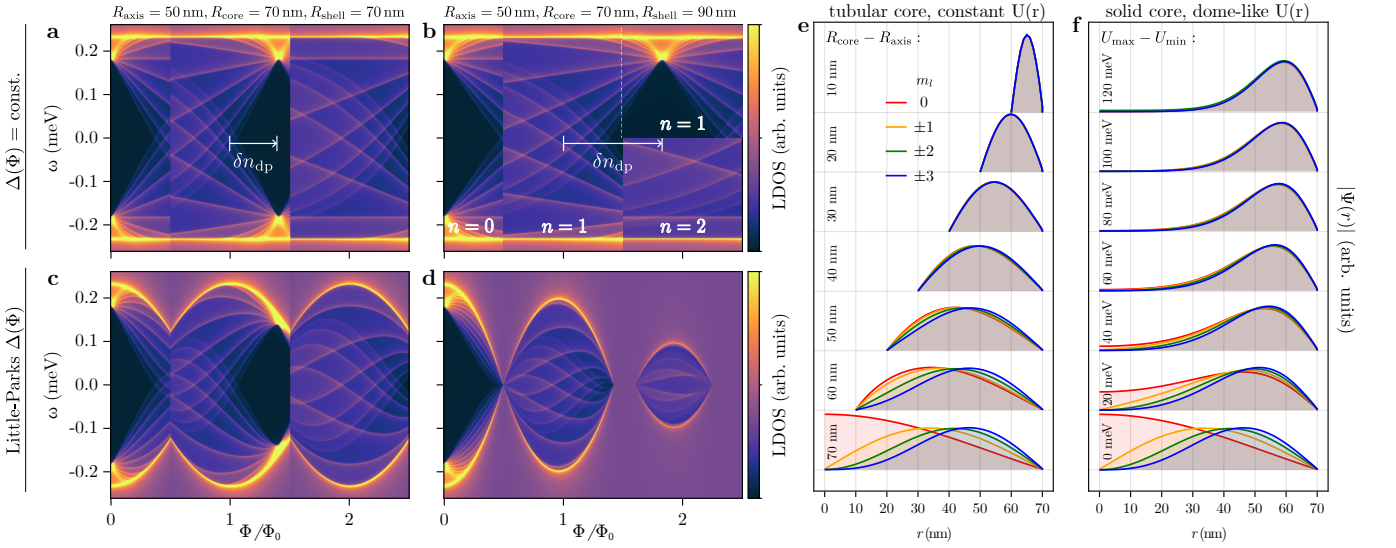


FIG. 6. (a) LDOS in arbitrary units vs energy and normalized flux for a full-shell tubular-core nanowire with $R_{\text{axis}} = 50$ nm and $R_{\text{core}} = R_{\text{shell}} = 70$ nm and with dimensionless core/shell coupling $\tau = 0.6$. The LP gap is forced to be flux-independent, $c_1 = c_2 = 0$. The degeneracy point in the 1st lobe shifts to the right by a quantity δn_{dp} with respect to the $n = 1$ lobe center. (b) Same as (a) but for $R_{\text{shell}} = 90$ nm. The positive-energy part of the LDOS 2nd lobe, enclosed by a white dashed box, has been artificially forced to maintain an $n = 1$ fluxoid to reveal the position of the meta-stable $n = 1$ degeneracy point. (c,d) Same as (a,b) but considering the correct LP gap modulation with flux [coherence length $\xi = 80$ nm, so that $c_1 = 1.90$, $c_2 = 0.0$ in (c) and $\xi = 180$ nm so that $c_1 = 3.84$, $c_2 = 0.152$ in (d)]. (e) Wavefunction modulus ($|\Psi(r)| = |\tilde{\Psi}(r)|$) of the lowest excitation at $k_z = 0$ in the normal state ($\tau = 0$) vs radial coordinate r for a tubular-core semiconducting nanowire of external radius $R_{\text{core}} = 70$ nm and different thicknesses, from $d_{\text{core}} = R_{\text{core}} - R_{\text{axis}} = 10$ nm at the top to 70 nm (solid core) at the bottom. Different (normal) angular momentum subbands m_l are marked with colors. (f) Same as (e) but for a solid-core semiconducting nanowire with a dome-like potential profile $U(r)$, see Eq. (23). Different values of $U_{\text{max}} - U_{\text{min}}$ from top to bottom are indicated (with $U_{\text{max}} = 0$ and exponent $\nu = 3$). Other parameters like in Fig. 5.

Al work function and the InAs electron affinity. The degree of band bending and precise shape of $U(r)$, however, depends on microscopic details of the interface and the equilibrium electrostatic screening. In keeping with the conceptual approach of our analysis, we will consider a simple model for $U(r)$ of the form

$$U(r) = U_{\text{min}} + (U_{\text{max}} - U_{\text{min}}) \left(\frac{r}{R_{\text{core}}} \right)^\nu, \quad (23)$$

see illustrations in Fig. 1(d) and Fig. 7(a). We will specialise our simulations with $\nu = 3$ and $U_{\text{max}} = 0$, with U_{min} ranging from -120 meV to -30 meV, as suggested by microscopic calculations^{1,36}. The solid-core nanowire BdG effective Hamiltonian in the m_L, k_z -rotated basis then reads

$$\tilde{H} = \left[\frac{(m_L - \frac{1}{2}n\tau_z + \frac{1}{2}\frac{\Phi}{\Phi_0}\tau_z)^2}{2m^*r^2} + \frac{k_z^2 + p_r^2}{2m^*} + U(r) \right] \tau_z + \Sigma_{\text{shell}}^{\text{1D}}(0). \quad (24)$$

B. LDOS and transport

Despite R_{axis} being zero in the solid-core model, we find that its LDOS, shown in Figs. 7(b-d) for $R_{\text{core}} =$

70 nm, behaves rather similarly to that of tubular-core nanowires with $R_{\text{core}} = 70$ nm and $R_{\text{axis}} = 30 - 50$ nm, Figs. 5(d-f). The reason is that the potential $U(r)$ tends to concentrate the wavefunction of the various m_l modes to a region closer to the core/shell interface. The precise wavefunction profile is shown in Fig. 6(f), which confirms that, indeed, all m_l modes exhibit a very similar shape, with an $R_{\text{av}} = 45 - 60$ nm for $R_{\text{core}} = 70$ nm that depends only weakly on the potential $U(r)$ for realistic values $U_{\text{min}} < -30$ meV. The main effect of increasing band bending (decreasing U_{min} to more negative values) is simply to increase the number of occupied m_l modes, and hence the number of CdGM Van Hoves visible within each lobe [compare Fig. 7(d) to Fig. 7(b)].

In experiments, the technique of choice to locally measure the subgap spectral structure of both full-shell and partial-shell devices has traditionally been tunnelling transport spectroscopy. The technique measures the differential conductance dI/dV from a normal probe at bias V coupled to a grounded hybrid nanowire across an externally tuneable barrier. For high and sharp barriers, it was shown that the tunnelling dI/dV becomes proportional to the BdG LDOS at the contact^{58,59}, hence the name tunnelling spectroscopy. We confirm this by computing the dI/dV in the non-interacting Green's function formalism across a sharp $L_b = 50$ nm-long Gaus-

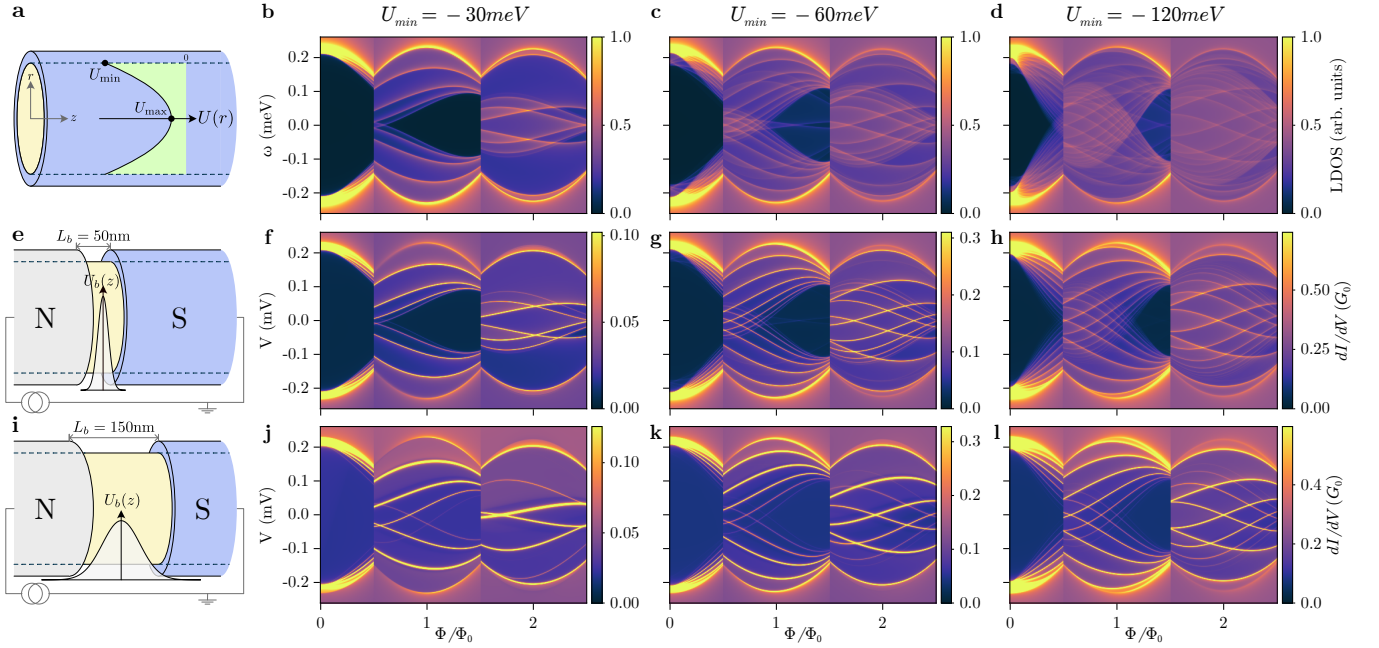


FIG. 7. (a) Schematics of a solid-core, full-shell, semi-infinite nanowire with semiconductor electrostatic potential $U(r)$ in its interior. (b-c) LDOS in arbitrary units vs energy and normalized flux for a $R_{\text{core}} = 70\text{nm}$, $R_{\text{shell}} = 80\text{nm}$ nanowire with $U_{\text{max}} = 0$ and different values of U_{min} , from a shallow (b) to a deep (d) dome-like profile. (e) Schematics of a full-shell nanowire-based normal-superconductor tunnel junction. The potential-barrier profile $U_b(z)$ in the uncovered semiconductor region between the normal metal (N) and the full-shell wire (S) only depends on z . (f-h) Differential conductance dI/dV (in units of the conductance quantum G_0) vs normalized flux for the same full-shell nanowires as in (b-d), and for a sharp tunnel barrier of width 50nm and height 60meV (f), 80meV (g) and 120meV (h). (i-l) Same as (e-l) but for a longer tunnel junction; width 150nm and heights 18meV (j), 38meV (k) and 80meV (l). Parameters: Column (b,f,j) has $\tau = 0.95$ and $a_0 = 10\text{nm}$; column (c,g,k) has $\tau = 0.85$ and $a_0 = 10\text{nm}$; and column (d,h,l) has $\tau = 0.65$ and $a_0 = 5\text{nm}$. Other parameters like in Fig. 5.

sian $U_b(z)$ barrier, with a normal probe defined using the same model as the solid-core nanowire but without the shell-induced $\Sigma_{\text{shell}}^{\text{1D}}$. The resulting dI/dV indeed matches closely the LDOS, see Fig. 7(f-h), with three notable differences caused by the small but finite L_b . First, Van Hove singularities appear much sharper in the dI/dV than in the LDOS, to the point that they could be easily mistaken for discrete levels. Second, a small particle-hole $V \rightarrow -V$ asymmetry is visible in dI/dV , whereas the BdG LDOS is symmetric by definition. Last, and most significant, the small but finite L_b makes the barrier more sensitive to modes with smaller $|m_L|$ [see m_L labels in Fig. 8(a), corresponding to the first lobe of Fig. 7(c)]. Depending on their m_L , different subbands are deeper or shallower, when plotted versus k_z . Their corresponding evanescent decay inside the barrier will then be slower or faster. Thus, barriers of finite length acquire a strong dependence of transmission probability with m_L .⁵⁸ As a result, Van Hove singularities with larger $|m_L|$ appear much fainter in the dI/dV , or they may even become undetectable.

All these deviations become exacerbated when we consider even longer barriers with realistic lengths $L_b \sim 150\text{nm}$, see Fig. 7(j-l). In this regime there is even a distinct deviation between the position of the CdGM ana-

log features relative to the LDOS. We argue that these deviations are the result of the distortion of the hybrid nanowire bulk states as they leak into the barrier region. In the limit of long L_b , the CdGM analogs can even transform into Andreev states localized around the barrier itself by repeated reflections between the barrier (normal) and the full-shell wire (normal and Andreev processes). In an experiment, such an occurrence should be relatively easy to detect, as the subgap features should acquire a significant energy dependence with barrier height, while genuine CdGM Van Hoves from the nanowire bulk should not.

We finally show in Fig. 8(b) the spatially-resolved LDOS across the center of the $n = 1$ lobe. This is closely related to the profile of core-states that were shown in Fig. 6(f), but this time including their coupling to the shell. As before, subgap states are concentrated around a certain R_{av} inside the core [see dashed line in panel 8(b)]⁶⁰. We can see that, except for states close to the gap edge, there is a rather small leakage of core states into the shell, even for $\tau = 1$ (perfect epitaxial contact). This is a result of the sizeable normal reflection due to the core/shell velocity mismatch that is built into our $\Sigma_{\text{shell}}^{\text{1D}}$ model. Note also the existence of other modes, particularly at low energy, with maxima away from R_{av} .

These correspond to higher radial momentum subbands, which may become populated in the lowest m_L sector for dense enough and/or thick enough nanowires.

V. ANALYTIC DESCRIPTION OF VAN HOVES

In this section we show that the essence of the CdGM Van Hove singularities can be captured by a simple analytical expression that combines the ideas developed in the preceding sections to yield their energy in terms of material and geometric parameters, see dashed lines in Fig. 8(a). The essence of the approach consists in replacing the realistic solid-core system with an effective hollow core nanowire of reduced radius $R_{\text{core}} = R_{\text{av}}$, but preserving the original R_{LP} in the definition of Φ .

Let us focus on the $n = 1$ sector. As analyzed above, the degeneracy point of Van Hove singularities occurs at $\Phi_{\text{dp}}/\Phi_0 = 1 + \delta n_{\text{dp}}$, where, recall, the non-zero shift δn_{dp} stems from the reduced R_{av} relative to the LP radius, see Eq. (22). At $\Phi = \Phi_{\text{dp}}$ the normal-state electron-hole subbands of the effective R_{av} hollow core cross at zero energy, see Fig. 3(d). As Φ moves away from the degeneracy point Φ_{dp} , the electron-hole crossing is also shifted away from zero energy as

$$\varepsilon(\Phi) = \left(\frac{\Phi}{\Phi_0} - 1 - \delta n_{\text{dp}} \right) t_{\text{av}} m_L, \quad (25)$$

where $t_{\text{av}} \approx 1/(2m^* R_{\text{av}}^2)$. This results from Eq. (13) with R_{core} replaced by R_{av} and no self-energy $\Sigma_{\text{shell}}(0)$. The proximity effect from $\Sigma_{\text{shell}}(0)$ will then split this finite energy crossing, producing flux-dependent Van Hove singularities. Their positions correspond approximately to poles ω_{VH} of the Nambu Green's function $G(\omega)$, whose inverse within the electron-hole subspace can be approximated in the Andreev limit as

$$G^{-1}(\omega) = \omega \begin{pmatrix} 1 & 0 \\ 0 & 1 \end{pmatrix} - \varepsilon(\Phi) \begin{pmatrix} 1 & 0 \\ 0 & 1 \end{pmatrix} - \frac{\Gamma_N}{\sqrt{\Delta(\Phi)^2 - \omega^2}} \begin{pmatrix} \omega & -\Delta(\Phi) \\ -\Delta(\Phi) & \omega \end{pmatrix}, \quad (26)$$

where the last term is the shell self-energy $\Sigma_{\text{shell}}^\infty(\omega)$, see Eq. (10), and Γ_N is the normal-state decay rate of the electron-hole sector into the shell.

The pole positions ω_{VH} are solutions of $\det(G^{-1}) = 0$. For solutions inside the gap $0 \leq \omega \leq \Delta$, this condition can be simplified to

$$(\Delta - \omega_{\text{VH}})\Gamma_N^2 = (\varepsilon - \omega_{\text{VH}})^2(\Delta + \omega_{\text{VH}}), \quad (27)$$

where we have omitted the implicit Φ dependence. The general solutions of this equation are rather complicated, since it is cubic in ω_{VH} , although they are easy to obtain numerically. Equation (27) also allows to extract several analytical results without explicitly solving it. We can derive, for example, the connection between Γ_N and

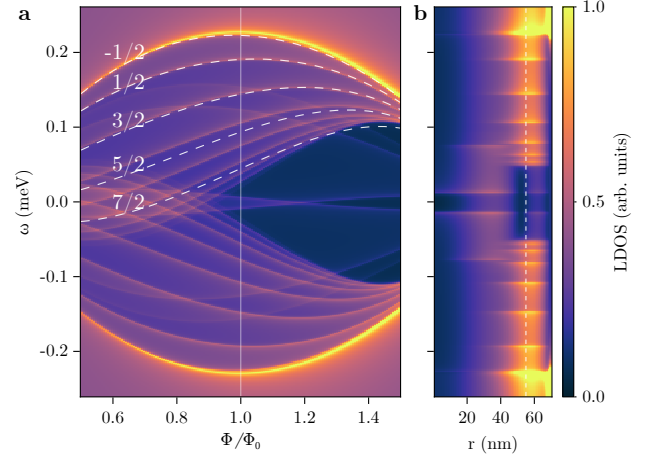


FIG. 8. (a) First LP lobe of Fig. 7(c). The analytical $\omega > 0$ solutions for the CdGM Van Hove singularities of Eq. (27) are plotted on top with a white dashed line, together with the value of the generalized angular momentum quantum number m_L . (b) Square root of LDOS in arbitrary units vs radial coordinate for the flux $\Phi = \Phi_0$ in (a). The white dashed line in (b) corresponds to the average radius $R_{\text{av}} = 55\text{nm}$.

$\Delta^* = \tau^* \Delta(0)$, since Δ^* is the ω_{VH} solution at $\Phi = 0$, where $\varepsilon = 0$. It reads

$$\Gamma_N = \Delta^* \sqrt{\frac{\Delta(0) + \Delta^*}{\Delta(0) - \Delta^*}} = \Delta^* \sqrt{\frac{1 + \tau^*}{1 - \tau^*}}. \quad (28)$$

We can also obtain an expression for the degeneracy point shift δn_{dp} in terms of the energy $\omega_1 = \omega_{\text{VH}}(\Phi = \Phi_0)$ of any Van Hove singularity at the center of the $n = 1$ lobe, and of its normalized slope $\omega'_1 = \Phi_0 \partial_\Phi \omega_{\text{VH}}|_{\Phi = \Phi_0}$. These two quantities should be easy to measure experimentally, and should yield a similar value of δn_{dp} for Van Hoves with different m_L , so long as they have an approximately equal R_{av} . The expression for δn_{dp} is obtained by evaluating Eq. (27) and its derivative respect Φ at $\Phi = \Phi_0$ and solving for m_L and δn_{dp} through Eq. (25),

$$(\Delta_1 - \omega_1)\Gamma_N^2 = (m_L t_{\text{av}} \delta n_{\text{dp}} + \omega_1)^2 (\Delta_1 + \omega_1), \quad (29)$$

$$\omega'_1 \Gamma_N^2 = 2(m_L t_{\text{av}} \delta n_{\text{dp}} + \omega_1)(\Delta_1 + \omega_1)(m_L t_{\text{av}} - \omega'_1) - (m_L t_{\text{av}} \delta n_{\text{dp}} + \omega_1)^2 \omega'_1. \quad (30)$$

Here we have denoted $\Delta(\Phi = \Phi_0) = \Delta_1$. The solution for δn_{dp} reads

$$\begin{aligned} \delta n_{\text{dp}} &= \frac{\Delta_1^2 - \omega_1^2}{\omega'_1} \\ &\times \frac{\Gamma_N \sqrt{\Delta_1^2 - \omega_1^2} - \omega_1 (\Delta_1 + \omega_1)}{\Gamma_N \Delta_1 \sqrt{\Delta_1^2 - \omega_1^2} + \Delta_1^3 + \Delta_1^2 \omega_1 - \Delta_1 \omega_1^2 - \omega_1^3} \\ &= \frac{R_{\text{LP}}^2}{R_{\text{av}}^2} - 1, \end{aligned} \quad (31)$$

where the last equality corresponds to Eq. (22).

The quality of our analytical treatment can be assessed by comparing the solution of Eq. (27) to the full numerical calculation in the solid-core nanowire model. Using the values for $\Delta(\Phi = \Phi_0)$, Δ^* and R_{LP} corresponding to Fig. 7(c), and fixing $R_{av} \approx 55\text{nm}$ as suggested by the spatial LDOS profile of Fig. 8(b), Eq. (27) yields the white dashed lines shown in Fig. 8(a) without any further fitting parameter, in rather reasonable agreement with the full numerical results.

VI. ROLE OF SPIN-ORBIT COUPLING AND ZEEMAN

Up to this point we have completely neglected SOC and Zeeman splittings in our models. SOC is a crucial ingredient in the context of topological superconductivity and MBSs, as it controls the magnitude of the topological gap. Without SOC, no localized Majoranas can arise in this type of systems. However, as we show in this section, the SOC does not have a significant effect on the rest of the subgap spectrum, whereas the Zeeman coupling produces only a small splitting of otherwise degenerate CdGM analog states.

The generalization of the Hamiltonian in Eq. (24) to include SOC was discussed in Ref. 1. It involves writing U in terms of the eigenvalues m_J of the total generalized angular momentum, $J_z = -i\partial_\varphi + \frac{1}{2}\sigma_z + \frac{1}{2}n\tau_z$ (instead of the m_L eigenvalues of the generalized orbital momentum L_z used up to this point). The m_J 's become good quantum numbers of the Hamiltonian eigenstates in the presence of SOC. The Zeeman effect can be included in the BdG Hamiltonian \tilde{H} by adding the term

$$V_Z = \frac{1}{2}g\mu_B B_z \sigma_z, \quad (32)$$

where μ_B is the Bohr magneton, and g is the nanowire Landé g -factor. Following this scheme, we computed the LDOS of a solid-core nanowire with and without Zeeman and SOC. We use a g -factor of 12 for our simulations, and a SOC of the form $\alpha(r)\hat{\mathbf{r}} \cdot (\boldsymbol{\sigma} \times \mathbf{p})$. Here $\alpha(r)$ is written, using a standard 8-band model⁶¹, in terms of the radial potential gradient $\partial_r U(r)$,

$$\alpha(r) = \alpha_0 \partial_r U(r) = \frac{eP^2}{3} \left[\frac{1}{\Delta_g^2} - \frac{1}{(\Delta_{\text{soff}} + \Delta_g)^2} \right] \partial_r U(r), \quad (33)$$

Using the parameters $P = 919.7\text{meV nm}^2$, $\Delta_g = 417\text{meV}$ and $\Delta_s = 390\text{meV}$ relevant to InAs, we obtain $\alpha_0 = 1.19\text{nm}^2$ (see Ref. 62 for more elaborate approximations).

The simulations are shown in Figs. 9(a,b) with $g = 0$ and Figs. 9(c,d) with finite g, α . In the two rows we choose different values of U_{min} that result in a topologically trivial and non-trivial phase for the $m_J = 0$ sector when adding SOC, see Figs. 9(c) and 9(d), respectively. In the latter we note that SOC indeed produces a sharp Majorana zero mode with $m_J = 0$ throughout

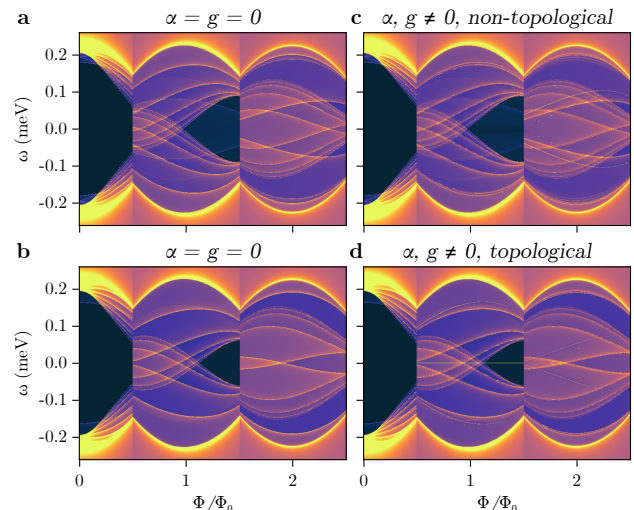


FIG. 9. (a,b) LDOS in arbitrary units vs energy and normalized flux at two different values of $U_{\text{min}} = -40\text{meV}$ and $U_{\text{min}} = -50\text{meV}$, respectively, with no SOC (α) or Zeeman (g). (c,d) The same configuration with a finite SOC and Zeeman, which correspond to non-topological and topological phases, respectively. All other parameters like the first row of Fig. 7, with $\tau = 0.8$.

the first lobe, as expected (recall that the nanowire is semi-infinite). More generally, SOC also introduces a few additional, rather sharp subgap features, while Zeeman produces a small splitting of each Van Hove peak. Overall, however, the rest of the CdGM spectrum remains almost unperturbed.

VII. DISCUSSION

We have shown that the CdGM of type-II superconductors have an analog in full-shell nanowires, made possible by fluxoid quantization in the LP effect. Although flux itself is not quantized as in an Abrikosov vortex, the integer winding number of the shell's pairing in nonzero LP lobes also stabilizes a variety of low-energy subgap states in the nanowire core. Despite the various differences mentioned in the introduction between the original CdGM states and their full-shell analogs, their essential nature is the same: subgap states resulting from two-dimensional confinement by a superconductor with a finite winding in its phase.

At a more detailed level, however, full-shell CdGM analogs are Van Hove singularities with a far richer structure. We have seen that their wavefunction within a cross section of the nanowire is ring-like, with its maximum concentrated around a finite radius R_{av} that depends on the shape of the dome-like potential profile within the superconductor. This turns out to have strong consequences in their behavior with flux Φ .

On the one hand, the degeneracy point (where all Van

Hove singularities merge) shifts towards larger absolute values of the threading flux for $n \neq 0$ lobes, even disappearing beyond the lobe edge as R_{av} decreases with respect to R_{core} (or as R_{LP} increases with respect to R_{core}). This shift leaves behind a bundle of Van Hove singularities that spans the whole LP gap for smaller values of $|\Phi|$ within the lobe, but that leaves a characteristically shifted gap for larger $|\Phi|$ values. The degeneracy point shift is proportional to n , so that the shifted gap is more visible in the $n = 1$ lobe and tends to disappear faster with decreasing R_{av} for $n \geq 2$, see Fig. 5 and the first row of Fig. 7.

On the other hand, due to their diamagnetic coupling, CdGM analogs disperse with a positive or negative slope depending on their angular momentum. For $\omega > 0$ states, this pushes negative angular momenta m_L towards the gap edge, leaving only $m_L > 0$ states below the LP gap edge that exhibit a systematic skewness towards high magnetic fields within nonzero LP lobes, see Fig. 8(a). The m_L quantum numbers of these $\omega > 0$ CdGM analog states are ordered from smaller to larger values from the LP gap edge at high energies towards zero energy. (The opposite happens for $\omega < 0$ states.) This is the opposite order than CdGM states at type-II vortex cores.

The number, energy and skewness of CdGM analogs in full-shell wires can be accessed using tunneling spectroscopy with sufficiently short tunnel barriers. These quantities can be used to obtain estimates of microscopic quantities such as the average wire's doping or the transparency of the core/shell interface. Using the analytical expressions developed in Sec. V we can even obtain the average radius R_{av} for the wavefunction of each mode. This highlights the rich information contained in CdGM analogs of otherwise inaccessible parameters of the shell-encapsulated semiconducting wire.

In samples with larger tunneling barriers, there is often the problem that quantum-dot-like states, localized around the barrier, appear within the gap. These are not part of the bulk nanowire spectrum, but depend on barrier details. It is possible experimentally to verify that a measured subgap feature in tunneling conductance is

indeed a CdGM analog, and not a quantum dot state, by checking that it is largely insensitive to changes in the tunnel barrier. CdGM analogs, as Van Hove singularities of the nanowire bandstructure, are associated to the extended bulk of the nanowire, not to local barrier details. Another two revealing characteristics of CdGM analogs are their skewness with flux and the presence of a shifted gap. For nanowires of finite-length L , they should still be detectable as a collection of longitudinally quantized levels with a level spacing $\sim 1/L$.

To conclude, we have shown that CdGM analogs are an unexpectedly effective probe into the microscopic details of full-shell nanowires, a very special type of hybrid structure with non-trivial physics and potential in the field of Majoranas. CdGM analogs contain a wealth of otherwise inaccessible information about their host system. This includes electron density, angular momentum of modes, wavefunction profiles or Andreev reflection processes inside the nanowire core. As we have shown in this work, simple models and concepts, such as degeneracy point shifts δn_{dp} and average radius R_{av} , make it possible to rationalize the complex spectral phenomenology of CdGM analogs, and exploit it to obtain some of this microscopic information through simple tunneling spectroscopy measurements. Our analysis remains robust when introducing additional complexity to the models, such as SOC, Zeeman splittings or even non-cylindrical sections of the nanowire.

ACKNOWLEDGMENTS

This research was supported by Grant Nos. FIS2017-84860-R, PGC2018-097018-B-I00, and PID2021-122769NB-I00 funded by MCIN/AEI/10.13039/501100011033 and by "ERDF A way of making Europe", the Comunidad de Madrid through Grant No. S2018/NMT-4511 (NMAT2D-CM), the Danish National Research Foundation, and a research grant (Project 43951) from VILLUM FONDEN.

¹ S. Vaitiekėnas, G. W. Winkler, B. van Heck, T. Karzig, M.-T. Deng, K. Flensberg, L. I. Glazman, C. Nayak, P. Krogstrup, R. M. Lutchyn, and C. M. Marcus, *Science* **367** (2020), 10.1126/science.aav3392.

² F. Peñaranda, R. Aguado, P. San-Jose, and E. Prada, *Phys. Rev. Research* **2**, 023171 (2020).

³ M. Valentini, F. Peñaranda, A. Hofmann, M. Brauns, R. Hauschild, P. Krogstrup, P. San-Jose, E. Prada, R. Aguado, and G. Katsaros, *Science* **373**, 82 (2021).

⁴ S. D. Escribano, A. Levy Yeyati, R. Aguado, E. Prada, and P. San-Jose, *Phys. Rev. B* **105**, 045418 (2022).

⁵ V. Mourik, K. Zuo, S. M. Frolov, S. R. Plissard, E. P. A. M. Bakkers, and L. P. Kouwenhoven, *Science* **336**, 1003 (2012).

⁶ P. Krogstrup, N. L. B. Ziino, W. Chang, S. M. Albrecht, M. H. Madsen, E. Johnson, J. Nygård, C. M. Marcus, and T. S. Jespersen, *Nat. Mater.* **14**, 400 (2015).

⁷ A. E. Antipov, A. Bargerbos, G. W. Winkler, B. Bauer, E. Rossi, and R. M. Lutchyn, *Phys. Rev. X* **8**, 031041 (2018).

⁸ B. D. Woods, T. D. Stanescu, and S. Das Sarma, *Phys. Rev. B* **98**, 035428 (2018).

⁹ G. W. Winkler, A. E. Antipov, B. van Heck, A. A. Soluyanov, L. I. Glazman, M. Wimmer, and R. M. Lutchyn, *Phys. Rev. B* **99**, 245408 (2019).

¹⁰ Y. Oreg, G. Refael, and F. von Oppen, *Phys. Rev. Lett.* **105**, 177002 (2010).

¹¹ R. M. Lutchyn, J. D. Sau, and S. Das Sarma, *Phys. Rev. Lett.* **105**, 077001 (2010).

- ¹² S. Vaitiekėnas, P. Krogstrup, and C. M. Marcus, Phys. Rev. B **101**, 060507(R) (2020).
- ¹³ D. Sabonis, O. Erlandsson, A. Kringhøj, B. van Heck, T. W. Larsen, I. Petkovic, P. Krogstrup, K. D. Petersson, and C. M. Marcus, Phys. Rev. Lett. **125**, 156804 (2020).
- ¹⁴ A. Kringhøj, G. W. Winkler, T. W. Larsen, D. Sabonis, O. Erlandsson, P. Krogstrup, B. van Heck, K. D. Petersson, and C. M. Marcus, Phys. Rev. Lett. **126**, 047701 (2021).
- ¹⁵ A. Vekris, J. C. Estrada Saldaña, J. de Bruijckere, S. Lorić, T. Kanne, M. Marnauza, D. Olsteins, J. Nygård, and K. Grove-Rasmussen, Scientific Reports **11**, 19034 (2021).
- ¹⁶ W. A. Little and R. D. Parks, Phys. Rev. Lett. **9**, 9 (1962).
- ¹⁷ R. D. Parks and W. A. Little, Phys. Rev. **133**, A97 (1964).
- ¹⁸ F. London, *Superfluids*, Vol. 1 (Wiley, New York, 1950).
- ¹⁹ M. Tinkham, *Introduction to superconductivity* (Courier Corporation, 2004).
- ²⁰ P.-G. De Gennes, *Superconductivity of metals and alloys* (CRC Press, 2018).
- ²¹ B. S. Deaver and W. M. Fairbank, Phys. Rev. Lett. **7**, 43 (1961).
- ²² R. Doll and M. Näbauer, Phys. Rev. Lett. **7**, 51 (1961).
- ²³ D. Einzel, J. Low Temp. Phys. **163**, 215 (2011).
- ²⁴ Y. Liu, Y. Zadorozhny, M. M. Rosario, B. Y. Rock, P. T. Carrigan, and H. Wang, Science **294**, 2332 (2001).
- ²⁵ I. Sternfeld, E. Levy, M. Eshkol, A. Tsukernik, M. Karpovskii, H. Shtrikman, A. Kretinin, and A. Palevski, Phys. Rev. Lett. **107**, 037001 (2011).
- ²⁶ M. Tinkham, Phys. Rev. **129**, 2413 (1963).
- ²⁷ N. Shah and A. Lopatin, Phys. Rev. B **76**, 094511 (2007).
- ²⁸ G. Schwiete and Y. Oreg, Phys. Rev. Lett. **103**, 037001 (2009).
- ²⁹ G. Schwiete and Y. Oreg, Phys. Rev. B **82**, 214514 (2010).
- ³⁰ C. Caroli, P. D. Gennes, and J. Matricon, Phys. Lett. **9**, 307 (1964).
- ³¹ E. Brun Hansen, Physics Letters A **27**, 576 (1968).
- ³² J. Bardeen, R. Kümmel, A. E. Jacobs, and L. Tewordt, Phys. Rev. **187**, 556 (1969).
- ³³ A. A. Kopašov and A. S. Mel'nikov, Phys. Rev. B **101**, 054515 (2020).
- ³⁴ N. B. Kopnin, A. S. Mel'nikov, V. I. Pozdnyakova, D. A. Ryzhov, I. A. Shereshevskii, and V. M. Vinokur, Phys. Rev. Lett. **95**, 197002 (2005).
- ³⁵ K. Tanaka, I. Robel, and B. Jankó, Proc. Nat. Ac. Sci. **99**, 5233 (2002).
- ³⁶ A. E. G. Mikkelsen, P. Kotetes, P. Krogstrup, and K. Flensberg, Phys. Rev. X **8**, 031040 (2018).
- ³⁷ C. Berthod, I. Maggio-Aprile, J. Bruér, A. Erb, and C. Renner, Phys. Rev. Lett. **119**, 237001 (2017).
- ³⁸ F. London, H. London, and F. A. Lindemann, Proc. R. Soc. Lond. **149**, 71 (1935).
- ³⁹ C. Kittel, P. McEuen, and P. McEuen, *Introduction to solid state physics*, Vol. 8 (Wiley New York, 1996).
- ⁴⁰ W. Meissner and R. Ochsenfeld, Naturwissenschaften **21**, 787 (1933).
- ⁴¹ H. Essén and M. C. N. Fiolhais, Am. J. Phys. **80**, 164 (2012), <https://doi.org/10.1119/1.3662027>.
- ⁴² N. Byers and C. N. Yang, Phys. Rev. Lett. **7**, 46 (1961).
- ⁴³ W. Brenig, Phys. Rev. Lett. **7**, 337 (1961).
- ⁴⁴ D. H. Douglass, Phys. Rev. **132**, 513 (1963).
- ⁴⁵ A. A. Abrikosov and L. P. Gor'kov, Zhur. Eksptl'. i Teoret. Fiz. **Vol: 39** (1960).
- ⁴⁶ V. H. Dao and L. F. Chibotaru, Phys. Rev. B **79**, 134524 (2009).
- ⁴⁷ J. Bardeen, Rev. Mod. Phys. **34**, 667 (1962).
- ⁴⁸ R. P. Groff and R. D. Parks, Phys. Rev. **176**, 567 (1968).
- ⁴⁹ N. C. Koshnick, H. Bluhm, M. E. Huber, and K. A. Moler, Science **318**, 1440 (2007), <https://www.science.org/doi/pdf/10.1126/science.1148758>.
- ⁵⁰ J. C. Cuevas, A. Martín-Rodero, and A. L. Yeyati, Phys. Rev. B **54**, 7366 (1996).
- ⁵¹ T. D. Stanescu and S. Das Sarma, Phys. Rev. B **96**, 014510 (2017).
- ⁵² Note the difference between m_L in this work and $m_J = m_L + s_z$ in Ref. 1. The reason is the lack of radial SOC in our case, which makes it unnecessary to transform the spin to diagonalize the Hamiltonian.
- ⁵³ S. Sanvito, C. J. Lambert, J. H. Jefferson, and A. M. Bratkovsky, Phys. Rev. B **59**, 11936 (1999).
- ⁵⁴ E. Prada and F. Sols, Eur. Phys. J. B **40**, 379 (2004).
- ⁵⁵ The absence of visibility in the LDOS of small momentum Van Hove singularities applies also to the $m_J = 0$ subband gap closing and reopening at $k_z = 0$ that occurs at the topological phase transition in the presence of SOC (not studied here).
- ⁵⁶ V. Arsoški, N. Čukarić, M. Tadić, and F. Peeters, Computer Physics Communications **197**, 17 (2015).
- ⁵⁷ I. Tan, G. L. Snider, L. D. Chang, and E. L. Hu, Journal of Applied Physics **68**, 4071 (1990), <https://doi.org/10.1063/1.346245>.
- ⁵⁸ J. Bardeen, Phys. Rev. Lett. **6**, 57 (1961).
- ⁵⁹ A. Melo, C.-X. Liu, P. Rožek, T. Ö. Rosdahl, and M. Wimmer, SciPost Phys. **10**, 37 (2021).
- ⁶⁰ A number of additional, low-lying states from higher *radial* subbands are visible, and occupy spatial positions closer to the nanowire axis.
- ⁶¹ R. Winkler, S. Papadakis, E. De Poortere, and M. Shayegan, *Spin-orbit coupling effects in two-dimensional electron and hole systems*, Vol. 191 (Springer, 2003).
- ⁶² S. D. Escibano, A. L. Yeyati, and E. Prada, Phys. Rev. Research **2**, 033264 (2020).